Supporting Information

Quantifying Transport, Geometrical and Morphological Parameters in Li-ion Cathode Phases using X-ray Microtomography

Thushananth Rajendra[1], Aashutosh N. Mistry[2,a], Prehit Patel[1], Logan J. Ausderau[1], Xianghui Xiao[3,†], Partha P. Mukherjee[2,b,*], George J. Nelson[1,c,*]

[1]Department of Mechanical & Aerospace Engineering, The University of Alabama in Huntsville, Huntsville, AL, USA

[2]School of Mechanical Engineering, Purdue University, West Lafayette, IN 47907, USA

[3]Advanced Photon Source, Argonne National Laboratory, Lemont, IL USA

[†]Current Affiliation: National Synchrotron Light Source II, Brookhaven National Laboratory, Upton, NY, USA

[a] ORCID: 0000 – 0002 – 4359 – 4975
[b] ORCID: 0000 – 0001 – 7900 – 7261
[c] ORCID: 0000 – 0002 – 1170 – 245X
[*] Corresponding authors: george.nelson@uah.edu (GJN), pmukherjee@purdue.edu (PPM)

1. X-ray Microtomography Sample Preparation

Two electrodes from each of the four manufacturing variants noted above were used as the source material for the μCT samples. Samples were cut from the same coin cell electrode set studied in prior X-ray nanotomography measurements[1]. Two approaches were applied in preparing samples for the μCT measurements. In the first approach samples were cut from the stock cathode, placed in a plastic pipette tip, and cast in epoxy. For the second approach samples were cut from the stock cathodes and stacked between layers of Kapton tape. For cathode 1 three samples were cut, stacked in this configuration and then imaged simultaneously. The same approach was taken for cathode 2. For cathode 3 four samples were cut, stacked in this configuration and then imaged simultaneously. The same approach was taken for cathode 4. Regions covering a consistent electrode area of 175.5 μm x 422.5 μm were extracted from the tomographic data for the samples noted, and segmentation and analysis was performed on those regions.

2. Image Reconstruction

In this study, a center finding approach was taken, reconstructing a single slice in which the center was varied by fixed increments. The center finding algorithm compares the reconstructed images to each other and the absence of artifacts was exploited to designate the correct center[2]. The second step was to normalize the image data to obtain reliable attenuation information. Equation 1 is used to normalize the image data. Here I_{raw} is raw image data, I_{white} is the image data with the white field measurements, is the image data with the absence of X-ray exposure[3].

$$I_{normalized} = \frac{I_{raw} - I_{dark}}{I_{white} - I_{dark}} \quad [1]$$

Following normalization ring and stripe artifacts were removed from the image data using algorithms developed by TomoPy[4]. Following ring and stripe removal phase data was retrieved based on the phase-contrast measurements. The algorithm uses both Pagannin-type[3] and Bronnikov-type filters[5] for single-distance phase retrieval[3]. The final step was to reconstruct the image data based on the computed center of rotation. The reconstruction process was carried out on all of the electrode samples shown in Table 1 of the main text.

3. Aligning Electrodes

A custom MATLAB script was used along with ImageJ to correct the vertical alignment of the electrodes in the reconstructed image. The region of interest was cropped to the electrode thickness in the reconstructed image and was rotated appropriately using ImageJ. To acquire the coordinates, the electrodes were rotated to vertically align the current collectors. Subsequently, ImageJ was used to obtain the change in horizontal displacements of the electrode position between the first and the last image slice with the current collector's position being used as the reference point. The displacements were taken over the number of slices and applied as input to the MATLAB script to translate the electrode image in the opposite direction. The alignment of the electrode was fixed accordingly to ensure that the boundaries of the electrode were defined appropriately.

4. Watershed Approach

The gray scale shown in Figure S1.a was already cropped and corrected for the translation shift using ImageJ and MATLAB. A mean filter with a radius of 2 pixels was applied to the gray scale image using ImageJ. The intent of applying a mean filter was to smooth the image and to remove mild ring artifacts that were present in the X-ray data. The histogram data of the sample electrode was then acquired through ImageJ to reveal the range of pixel values that bound the different phases. The active material was of primary interest in the first segmentation technique, with a gray value in the range between ~8000 and 65535 on a 16-bit scale. The minimum value (~8000) between all the pixels in the image was obtained through the histogram and a minimum mathematical function was carried out on the image using ImageJ. This technique cleared out most of the surrounding regions except for the active material and the current collector as shown in Figure S1.b. The general thresholding routine was carried out in ImageJ that resulted in a binary image shown in Figure S1.c. The white regions are classified as the active material (NMC particles) while the regions surrounding them are classified as open spaces (binder/carbon, current collector, tape and macro pores). Following the result as a binary image, the segmentation process was carried out using ImageJ. Some of the NMC particles had holes and cracks because of fracture and internal stresses due to lithiation, a Fill-hole function was applied on the image to retrieve the particles as shown in Figure S1.d. The watershed segmentation carried through ImageJ did not initially yield a good result; certain NMC particles were either over or under-segmented. Because of this issue, morphological image processing techniques were implemented prior to the watershed method. Ebner et al. highlights the use of ultra-erosion technique to extract locations of the tagged particles[6]. A similar approach was followed while eroding the voxels; however, the voxels were dilated after the segmentation to retrieve the voxels lost during the image erosion. Previously, the implementation of both erosion and dilation was applied to extract contact area between the secondary phases and the active material in LiCoO2 cathodes[7]. Figure S1.e shows the application of image erosion on the tomographic data. This technique was followed by the watershed method shown in Figure S1.f. The image was then dilated and multiplied with the original threshold image to retrieve back the holes as shown in Figure S1.g. This image illustrates the final segmented binary image used for characterization and further analysis. The combination of erosion, watershed segmentation and dilation allowed the particles to be separated with reduced instances of over and under segmentation. Figure S1.h shows the tagged version of the segmented image clearly defining the separation of the NMC particles. The tagged version was created by running a morphological segmentation on the segmented image using ImageJ.

5. Application of Phase contrast data

The active material was already separated from the region of interest using the previous watershed segmentation technique. The targeted regions for the following segmentation approach are the macro pores and the carbon/binder domain. To carry out this segmentation process, the phase contrast data of the image was extracted, and the phases were threshold based on their corresponding pixel value. Figure S2 shows the process carried out on the reconstructed cathode image. Initially, as shown in Figure S2.a, a mean filter of 1 pixel was added to the reconstructed image. This resulted image was followed by adjusting the brightness/contrast of the image using ImageJ (Figure S2.b), the above method allows the pixels to be saturated at

specific locations allowing regions with dark pixel values to be classified as macro pores while regions with light pixel values were classified as current collector, encapsulating tape or the carbon/binder domain. Once this step was achieved, the resulting image was multiplied by the inverted active material domain to eliminate the active material from the electrode region as shown in Figure S2.c. The current collector and the encapsulating tape surrounding the porous electrode were not of any importance in this study; therefore, it was vital to remove them from the processed image. This process was done using the Subtract Command in ImageJ (Figure S2.c). The Subtract Command uses the "rolling ball" algorithm[8] to remove smooth, continuous range of pixels from the image. The current collector and the encapsulating tape regions have a consistent range of pixel values in which some of the pixel values matched to that of the binder/carbon regions. By implementing the rolling ball algorithm in the electrode image, the pixel values of the current collector and the encapsulating tape were augmented allowing the pore and binder/carbon regions to be defined appropriately for further thresholding. The current collector and the encapsulating tape regions were removed by thresholding the image shown in Figure S2.c. This operation resulted in two particular regions- the electrode domain and the current collector/tape region (Figure S2.d). After Image processing, the image was loaded in MATLAB and the thresholding algorithm was implemented. The input for the script included the active material domain, electrode domain and the final processed image (Figure S2.d). The threshold value was obtained using the ImageJ line plot function. The pixel value that distinguishes the macro pore from the carbon/binder domain was used as the criteria. The holes and fractured regions in the active material were treated as macro pores. The regions between adjacent active materials were treated as binder considering the fact that the binder held the particles together. The script outputs the respective image files for the macro pore regions, carbon/binder domain and a combined domain (Figure S2.e). The white, dark gray, light gray and black regions were defined as the active material, pore space, carbon/binder domain and current collector/tape region respectively. The macro pore and the carbon/binder domain were extracted to evaluate the transport characteristics for the electrolyte in the porous electrode.

6. Particle Size Distribution

The particle size distribution (PSD) was implemented in FIJI; particles surrounding the border were excluded from the analysis because their inclusion would imply a known particle shape. These edge particles also exhibit a tendency to yield errant sphericity values greater than 1. The particle size distribution estimates the radius of the sphere with the same volume as the non-spherical particle. The algorithm computes the particle volume by counting the number of voxels occupied by each particle, the radius is then determined based on spheres of equivalent volume, subsequently, the radius is used to determine surface area. The algorithm implemented in ImageJ outputs particle count, radius, surface area and volume. These parameters were obtained to calculate particle sphericity(ψ), using Equation 2, characteristic length (L_c) using Equation 3 and specific surface area (SSA) using Equation 4. Here, V is particle volume and A is particle surface area. The specific surface area was calculated by taking the inverse of the characteristic length. The sphericity describes how close the particles represent to that of a perfect sphere. The

equation for sphericity was derived using the radius obtained from a sphere with the same volume as a non- spherical particle; however, this phase size radius was overestimated in the porous medium[1]. The characteristic length defines the ratio of the volume available for lithium ion storage to the area available for surface charge transfer.

$$\psi = \frac{\pi^{\frac{1}{3}}(6V)^{\frac{2}{3}}}{A} \quad [2]$$

$$L_c = \frac{V}{A} \quad [3]$$

$$SSA = \frac{A}{V} \quad [4]$$

7. Porosity Fraction calculation

The segmented phase contrast data of the electrode 3D tomogram was used to evaluate the porosity fraction of the four differently processed electrodes. Once the pore regions were defined appropriately followed by removing the redundant phase regions, Equation 5 was used in calculating the pore volume fraction. Here, NMC_x is defined as the number of voxels occupying the active material in the defined region of interest, ε_x is the number of voxels occupying the pore spaces in the defined region of interest, B_x is the number of voxels occupying binder/carbon domain in the defined region of interest and ε is the pore fraction of the medium.

$$\epsilon = \frac{\epsilon_x}{\epsilon_x + NMC_x + B_x} \quad [5]$$

8. Tortuosity Calculations

Pore phase tortuosity characterizes the connectivity of the electrolyte-filled pore network and its influence on the ionic transport. In an electrolyte-filled pore network, appropriate transport properties become a function of intrinsic electrolyte properties and the appropriate geometrical arrangement:

$$\psi_{eff} = \psi_0 \frac{\varepsilon}{\tau} \quad [6]$$

where ψ_0 is the intrinsic property such as electrolyte diffusivity, ionic conductivity and diffusional conductivity. Porosity, ε, is directly estimated from the tomography data, while tortuosity, τ, estimation is more involved. Tortuosity accounts for the geometrical aspects of ionic pathways including both their convoluted arrangement as well as constriction. Given such complications, tortuosity cannot be simply interpreted based on the path lengths. A consistent interpretation of tortuosity is offered as a solution of the concentration balance in the pore phase:

$$D\left(\frac{\partial^2 C}{\partial x^2}+\frac{\partial^2 C}{\partial y^2}+\frac{\partial^2 C}{\partial z^2}\right)=0 \qquad [7]$$

The above expression is solved at the pore scale. Tortuosity is a direction property and accordingly tortuosity estimation in each of the direction of interest requires different boundary conditions for the solution of [7]. For example, in order to solve for tortuosity in the *x*-direction, the following boundary conditions are ensured:

At $x = 0$: $C = C_{high}$ [8]

At $x = L_x$: $C = C_{low}$ [9]

At lateral faces: $\partial C / \partial n = 0$ [10]

where *n* is local surface normal pointing outwards. The governing equation [7] is solved subject to the set of boundary conditions [8] – [10] in a finite volume solver. Once the steady state concentration field (Figure 2.g of the main text) is obtained, tortuosity is estimated from the following identity:

$$J=-\frac{1}{A}\int D\frac{\partial C}{\partial x}\bigg|_{x=0}\mathrm{d}A=-D\frac{\varepsilon}{\tau}\left(\frac{C_{low}-C_{high}}{L_x}\right)=-\frac{1}{A}\int D\frac{\partial C}{\partial x}\bigg|_{x=L_x}\mathrm{d}A \qquad [11]$$

Similarly, tortuosities in other directions are obtained by appropriately setting the boundary conditions.

Solid phase conductivity is also a relevant transport property, outlining the effectiveness of electronic conduction. It is obtained as a solution of the electron conduction equation in the solid phases (with appropriate conductivities assigned to respective phases):

$$\frac{\partial}{\partial x}\left(\sigma\frac{\partial \phi}{\partial x}\right)+\frac{\partial}{\partial y}\left(\sigma\frac{\partial \phi}{\partial y}\right)+\frac{\partial}{\partial z}\left(\sigma\frac{\partial \phi}{\partial z}\right)=0 \qquad [12]$$

Here ϕ is solid phase electric potential, and σ is bulk material conductivity. Boundary condition treatment is similar to the tortuosity calculations. For example, in order to estimate the effective electronic conductivity in *x*-direction, the following set of boundary conditions are used:

At $x = 0$: $\phi = \phi_{high}$ [13]

At $x = L_x$: $\phi = \phi_{low}$ [14]

At lateral faces: $\partial \phi / \partial n = 0$ [15]

Once the steady state potential field is obtained (Figure 2(h) of the main text), the effective electronic conductivity is estimated via the following expression:

$$J = -\frac{1}{A}\int \sigma \left.\frac{\partial \phi}{\partial x}\right|_{x=0} \mathrm{d}A = -\sigma_{eff}\left(\frac{\phi_{low} - \phi_{high}}{L_x}\right) = -\frac{1}{A}\int \sigma \left.\frac{\partial \phi}{\partial x}\right|_{x=L_x} \mathrm{d}A \qquad [16]$$

Similar calculations are carried out in other coordinate directions as well.

Such effective property calculations are carried out over large enough spatial regions that allow the porous medium approximation, i.e., representative volume elements (RVEs; Figure 2.b of the main text). However, the electrode size is much larger than the RVE dimensions (Figure 2.a of main text). An ongoing challenge is to estimate effective properties for the entire tomographed region. Given the larger dimensions of the entire imaged volume, it is computationally ineffective to carry out calculations for the entire electrode volume. The definition of RVE allows a more effective approach. RVE is a suitable dimension that allows one to make the effective medium approximation. The entire electrode volume can be suitably divided into multiple non-overlapping RVEs and each can be characterized in the same fashion as described earlier. Consider the thickness direction. The flux going into the entire electrode volume is a combination of RVE scale fluxes. It can be shown that for the same fixed concentrations at the two ends, the following identity holds:

$$J_{electrode} = -D\frac{\varepsilon}{\tau}\left(\frac{C_{low} - C_{high}}{L_x}\right) = \frac{1}{N_{RVE}}\sum J_{RVE} = -\frac{1}{N_{RVE}}\sum D\frac{\varepsilon_{RVE}}{\tau_{RVE}}\left(\frac{C_{low} - C_{high}}{L_x}\right)$$

$$\therefore \frac{\varepsilon}{\tau} = \frac{1}{N_{RVE}}\sum \frac{\varepsilon_{RVE}}{\tau_{RVE}} \qquad [17]$$

Similarly, for the effective electronic conductivity, the electrode scale property is related to RVE scale values via:

$$\sigma_{eff} = \frac{1}{N_{RVE}}\sum \sigma_{eff,RVE} \qquad [18]$$

9. Numerical Modeling of Intercalation

The distribution for the mesh was predefined with 125 elements and a growth rate of 0.25 specified at the both ends of the electrode. The distribution of the mesh is fixed with 40 elements at the separator domain. The distribution was established based on the expected level of electrochemical activity occurring at these domains. All physical and geometrical parameters are presented in Table 1S.

The governing equations and boundary conditions were set following the Newman model as outlined by Doyle et al.[9]. The model is set up assuming that the active particles are representative spherical particles with a radius defined as the median radius for the given electrode. The mass balance for the Li ions in an active solid particle is given by Fick's second law in spherical coordinates:

$$\frac{\partial c_{s,i}}{\partial t} = D_{s,i}\frac{1}{r^2}\frac{\partial}{\partial}(r^2\frac{\partial c_{s,i}}{\partial r}) \qquad [19]$$

where r is the radius of the particle, i = p for positive electrode and i = n for negative electrode. Boundary conditions for the mass balance in a solid spherical particle are shown below.

At the center of the particle, the flux is given by the Equation 20 below. At the surface of the particle, the flux is given by Equation 21 below. The flux moving out from the surface of the particle is equal to the Lithium-ion consumed or produced during the electrochemical reaction, where J is pore wall flux of lithium ions moving outward from the active particle.

$$r = 0\,, \quad -D_{s,i}(\frac{\partial c_{s,i}}{\partial r}) = 0 \qquad [20]$$

$$r = R_{s,i}\,, \quad -D_{s,i}(\frac{\partial c_{s,i}}{\partial r}) = J_i \qquad [21]$$

The mass balance for the electrolyte in the liquid state is given by the Equation 22. This balance is applied for separator, the positive electrode and the negative electrode with i indicating the relevant domain and a_i representing the electrode surface area. For the separator region $J_i = 0$.

$$\varepsilon_i\frac{\partial c_i}{\partial t} = D_{eff,i}\frac{\partial^2 c_i}{\partial x^2} + (1 - t_+^0)\, a_i J_i \qquad [22]$$

At both ends of the cell, there is no flux so boundary conditions for both ends are given by equations below.

$$-D_{eff,p}\,(\frac{\partial c_p}{\partial x})_{x=0} = 0 \qquad [23]$$

$$-D_{eff,p}\,(\frac{\partial c_p}{\partial x})_{x = L_p + L_s + L_n} = 0 \qquad [24]$$

At the junction between the negative electrode - separator and the positive electrode - separator the concentration of the electrolyte and flux is continuous. The equations below represent the continuity in the concentration of electrolyte and flux in the cell.

$$(C_p)_{x\,=\,L_p^+} \;=\; (C_s)_{x\,=\,L_p^-} \qquad [25]$$

$$(C_s)_{x\,=\,(L_p\,+\,L_s)^-} \;=\; (C_n)_{x\,=\,(L_p\,+\,L_s)^+} \qquad [26]$$

$$-D_{eff,p}\,(\frac{\partial c_p}{\partial x})_{x=L_p^-} = -D_{eff,s}\,(\frac{\partial c_s}{\partial x})_{x=L_p^+} \qquad [27]$$

$$-D_{eff,s}\left(\frac{\partial c_s}{\partial x}\right)_{x=(L_p+L_s)^-} = -D_{eff,n}\left(\frac{\partial c_n}{\partial x}\right)_{x=(L_p+L_s)^-} \quad [28]$$

The effective diffusion coefficient of the electrolyte in the liquid phase is corrected by porosity given in Equation 29 below.

$$D_{eff,i} = D_i\frac{\varepsilon_i}{\tau_i} \quad [29]$$

The charge balance in the solid phase is determined using Ohm's law

$$-\sigma_{eff,i}\frac{\partial^2\varphi_{1,i}}{\partial x^2} = a_i F J_i \quad [30]$$

where F is Faraday's constant, φ is the potential in solid phase, and σ_{eff} is the effective conductivity. The effective conductivity is determined using the Equation 31 below.

$$\sigma_{eff,i} = \sigma_i\frac{\varepsilon_i}{\tau_i} \quad [31]$$

The charge flux at the junction of the current collector and the positive electrode is equal to the current density applied to the cell initially.

$$-\sigma_{eff,p}\left(\frac{\partial\varphi_{1,p}}{\partial x}\right)_{x=0} = i_{app} \quad [32]$$

The boundary conditions at the junction of the negative electrode - separator and positive electrode – separator are given below.

$$-\sigma_{eff,p}\left(\frac{\partial\varphi_{1,p}}{\partial x}\right)_{x=L_p} = 0 \quad [33]$$

$$-\sigma_{eff,n}\left(\frac{\partial\varphi_{1,n}}{\partial x}\right)_{x=L_p+L_s} = 0 \quad [34]$$

The potential of solid phase at the positive current collector was set to zero and the potential of the solid phase at the negative current collector is due to the applied current density. The charge balance for the electrolyte in the liquid phase is determined using Ohm's law in the Equation 35 below.

$$-\frac{\partial}{\partial x}\left(k_{eff,i}\frac{\partial\varphi_{2,i}}{\partial x}\right) + \frac{2RT\,(1-t_+^0)}{F}\frac{\partial}{\partial x}\left(k_{eff,i}\frac{\partial lnc_i}{\partial x}\right) = a_i F J_i \quad [35]$$

Where k_{eff} is specific conductivity of the binary electrolyte and i stands for separator, the positive electrode and the negative electrode. The specific conductivity k_{eff} can be calculated using Equation 36 below.

$$k_{eff,i} = k_i \frac{\varepsilon_i}{\tau_i} \quad [36]$$

At both the ends of the cell there is no charge flux in the liquid phase so the boundary conditions for both the ends are given by the equations below.

$$-k_{eff,p}\left(\frac{\partial \varphi_{2,p}}{\partial x}\right)_{x=0} = 0 \quad [37]$$

$$-k_{eff,n}\left(\frac{\partial \varphi_{2,n}}{\partial x}\right)_{x=L_p+L_s+L_n} = 0 \quad [38]$$

The pore wall flux J_i can be obtained by using Bulter-Volmer shown in Equation 39 given below.

$$J_i = k_i\left(c_{s,i,max} - c_{s,i,surf}\right)^{\alpha_a} c_{s,i,surf}^{\alpha_c} c_i^{\alpha_a}\left(exp\left(\frac{\alpha_a F}{RT}\eta_i\right) - exp\left(\frac{\alpha_c F}{RT}\eta_i\right)\right) \quad [39]$$

where η is the surface over potential and can be calculated using the Equation 40 below

$$\eta_i = \varphi_{1,i} - \varphi_{2,i} - U_i \quad [40]$$

where $\varphi_1$represents the potential in the solid phase, $\varphi_2$represents the solution potential and U represents the open circuit potential under the reference temperature.

The C-rate was varied between 1C and 5C for a normal discharge behavior (Figure 5-Main manuscript) and varied between 10C and 20C to understand the impact of aggressive C-rate on the electrode performance. Figure S3 illustrates the effect of aggressive C-rate on the capacity of the electrodes.

Figures and Tables

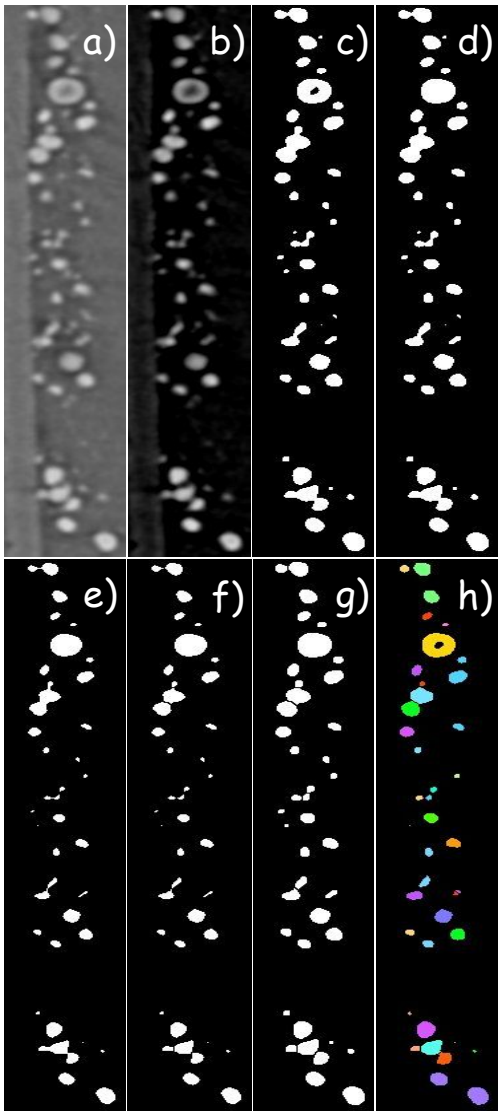

Figure S1. Method to segment Active material. a) Reconstructed image b) Minimum operation c) Thresholding image d) Fill hole operation e) Erosion operation f) Watershed operation g) Dilation operation and Multiplication with threshold image h) Morphological segmentation.

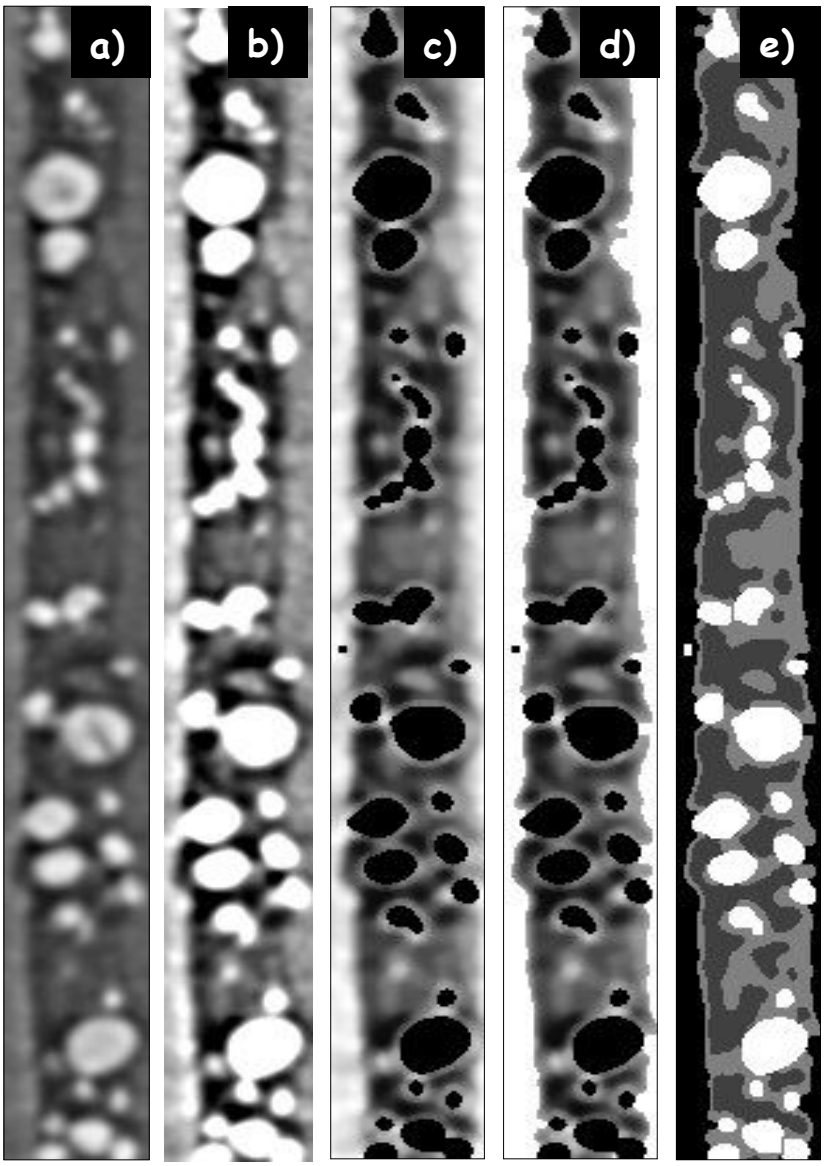

Figure S2. a) Mean filter on reconstructed image b) Adjust brightness/contrast to obtain phase contrast data c) Multiply image B with Active Material domain (Previous segmentation) d) Threshold the current collector/tape (white region) e) Thresholding technique to distinguish the different phases: Active material (White), Macropores(Dark grey), Carbon/Binder domain (Light Gray) and Current Collector/tape(Black).

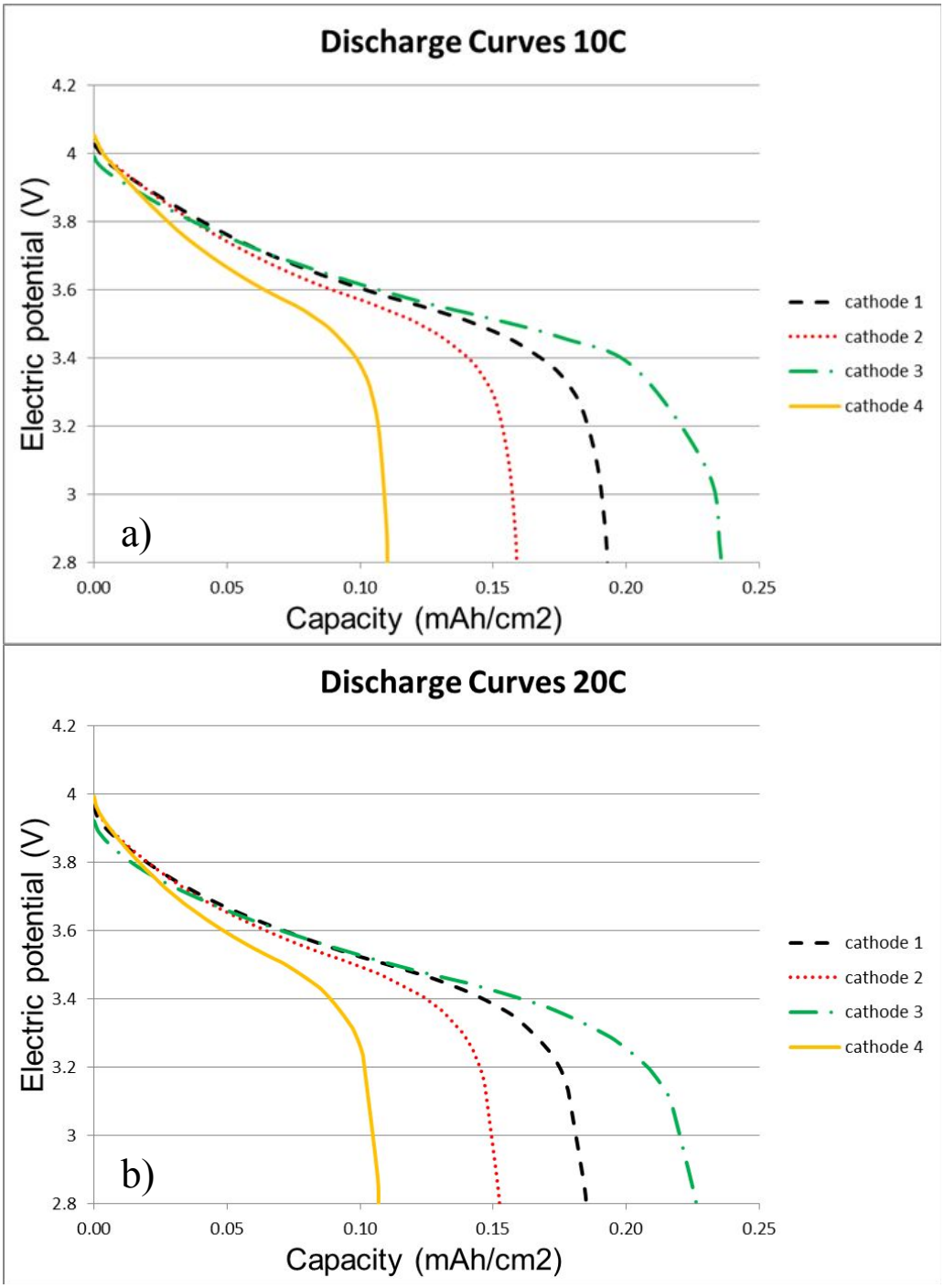

Figure S3. Discharge rate for the NMC cathodes. a) 10C b) 20C. Increasing the discharge rate decreases the capacity of the cathode.

Table S1. List of parameters applied in the pseudo-2D finite element model[1,9,10]

Parameter	Description	Value
$D_{neg}[m^2 s^{-1}]$	Solid phase Li-diffusivity of negative electrode (Li_xC_6)	3.9 x 10^{-14}
$D_{pos}[m^2 s^{-1}]$	Solid phase Li-diffusivity of positive electrode (NMC)	5 x 10^{-14}
$D_{separator}[m^2 s^{-1}]$	Solid phase diffusivity of separator	9 x 10^{-11}
$\sigma_{neg}[S m^{-1}]$	Solid phase conductivity of negative electrode	100
$\sigma_{pos}[S m^{-1}]$	Solid phase conductivity of positive electrode	10
$C_{L0}[mol m^{-3}]$	Initial electrolyte salt concentration	1000
$C_{s0\_neg}[mol m^{-3}]$	Initial concentration of lithium in solid phase negative electrode	14870
$C_{s0\_pos}[mol m^{-3}]$	Initial concentration of lithium in solid phase positive electrode	2286
$C_{smax\_neg}[mol m^{-3}]$	Maximum concentration of lithium in solid phase negative electrode	26390
$C_{smax\_pos}[mol m^{-3}]$	Maximum concentration of lithium in solid phase positive electrode	22860
L_{pos1}[m]	Thickness of positive electrode (cathode 1)	2.445 x 10^{-5}
L_{neg1}[m]	Thickness of negative electrode (anode 1)	4.056 x 10^{-5}
L_{sep}[m]	Thickness of separator	2.00 x 10^{-5}
α_c	Reaction rate coefficient negative electrode	0.5
α_a	Reaction rate coefficient positive electrode	0.5
C[C]	C-rate	1 , 5
t_+^0	Lithium transference number	0.363
T[K]	Temperature	298
$A_{cell}[m^2]$	Cell cross section area	7.415 x 10^{-8}

References

(1) Nelson, G. J.; Ausderau, L. J.; Shin, S.; Buckley, J. R.; Mistry, A.; Mukherjee, P. P.; De Andrade, V. Transport-Geometry Interactions in Li-Ion Cathode Materials Imaged Using X-Ray Nanotomography. J. Electrochem. Soc. 2017, 164, A1412–A1424. https://doi.org/10.1149/2.0261707jes.

(2) Donath, T.; Beckmann, F.; Schreyer, A. Automated Determination of the Center of Rotation in Tomography Data. J. Opt. Soc. Am. A Opt. Image Sci. Vis. 2006, 23, 1048–1057.

(3) Paganin, D.; Mayo, S. C.; Gureyev, T. E.; Miller, P. R.; Wilkins, S. W. Simultaneous Phase and Amplitude Extraction from a Single Defocused Image of a Homogeneous Object. J. Microsc. 2002, 206, 33–40. https://doi.org/10.1046/j.1365-2818.2002.01010.x.

(4) Gürsoy, D.; De Carlo, F.; Xiao, X.; Jacobsen, C. TomoPy: A Framework for the Analysis of Synchrotron Tomographic Data. J. Synchrotron Radiat. 2014, 21, 1188–1193. https://doi.org/10.1107/S1600577514013939.

(5) Bronnikov, A. V. Reconstruction Formulas in Phase-Contrast Tomography. Opt. Commun. 1999, 171, 239–244. https://doi.org/10.1016/S0030-4018(99)00575-1.

(6) Ebner, M.; Geldmacher, F.; Marone, F.; Stampanoni, M.; Wood, V. X-Ray Tomography of Porous, Transition Metal Oxide Based Lithium Ion Battery Electrodes. Adv. Energy Mater. 2013, 3, 845–850. https://doi.org/10.1002/aenm.201200932.

(7) Hutzenlaub, T.; Thiele, S.; Zengerle, R.; Ziegler, C. Three-Dimensional Reconstruction of a LiCoO2 Li-Ion Battery Cathode. Electrochem. Solid-State Lett. 2012, 15, A33. https://doi.org/10.1149/2.002203esl.

(8) Hui-Yan Jiang; Zhen-Yu Cheng; Yan Huo; Xiao-Jie Zhou; Tian-You Chai. Research on Image Denoising Methods Based on Wavelet Transform and Rolling-Ball Algorithm; IEEE, 2007; pp 1604–1607. https://doi.org/10.1109/ICWAPR.2007.4421708.

(9) Doyle, M. Modeling of Galvanostatic Charge and Discharge of the Lithium/Polymer/Insertion Cell. J. Electrochem. Soc. 1993, 140, 1526. https://doi.org/10.1149/1.2221597.

(10) Wiedemann, A. H.; Goldin, G. M.; Barnett, S. A.; Zhu, H.; Kee, R. J. Effects of Three-Dimensional Cathode Microstructure on the Performance of Lithium-Ion Battery Cathodes. Electrochimica Acta 2013, 88, 580–588. https://doi.org/10.1016/j.electacta.2012.10.104.